Journal of Catalysis 408 (2022) 423–435

Contents lists available at ScienceDirect

Journal of Catalysis

journal homepage: www.elsevier.com/locate/jcat

Elucidating the structure of the W and Mn sites on the Mn-Na_2WO_4/SiO_2 catalyst for the oxidative coupling of methane (OCM) at real reaction temperatures

Carlos A. Ortiz-Bravo [a,*], Santiago J.A. Figueroa [b], Raquel Portela [c], Carlos A. Chagas [d], Miguel A. Bañares [c,*], Fabio Souza Toniolo [a,*]

[a] Chemical Engineering Program of COPPE, Federal University of Rio de Janeiro, Rio de Janeiro 21941-972, Brazil
[b] Brazilian Synchrotron Light Laboratory (LNLS), Brazilian Center for Research in Energy and Materials (CNPEM), Campinas 13083-970, Brazil
[c] Institute of Catalysis and Petrochemistry (ICP), CSIC, Marie Curie 2, E-28049 Madrid, Spain
[d] School of Chemistry, Federal University of Rio de Janeiro, Rio de Janeiro 21941-909, Brazil

ARTICLE INFO

Article history:
Received 21 February 2021
Revised 13 June 2021
Accepted 25 June 2021
Available online 28 June 2021

Keywords:
Methane
OCM
Active sites
XANES
XAS
Raman
In situ

ABSTRACT

The performance of the Mn-Na_2WO_4/SiO_2 catalyst for oxidative coupling of methane (OCM) has been ascribed to crystalline phases that are not present at reaction temperatures (>700 °C). The evolution of W and Mn sites structure was monitored via *in situ* TPO-XRD, -Raman, and -XANES spectroscopies. TPO-XRD shows that the crystalline phases identified on the Mn-Na_2WO_4/SiO_2, Na_2WO_4/SiO_2, and WO_3/SiO_2 catalysts at room temperature do not exist at relevant OCM temperatures. The $\gamma \rightarrow \beta \rightarrow \alpha$-$WO_3$, $\alpha \rightarrow \beta$-cristobalite, and cubic → orthorhombic → molten-Na_2WO_4 phase transitions occur upon heating. TPO-Raman spectra show that the bond order of W sites with octahedral (O_h) and tetrahedral (T_d) symmetry changes during the $\delta \rightarrow \gamma \rightarrow \beta \rightarrow \alpha$-$WO_3$ and cubic → orthorhombic → molten-Na_2WO_4 transitions, respectively. TPO-XANES spectra show that bond order changes are due to distortion degree variations because all samples preserve essentially W^{6+} valence and O_h-Mn^{3+} sites are always present on Mn-Na_2WO_4/SiO_2 catalyst. Steady-state OCM tests show that O_h-W^{6+} sites are inactive and T_d-W^{6+} sites are less distorted and more active towards methane activation in the presence of O_h-Mn^{3+} sites.

1. Introduction

The increasing reserves of natural gas and the lack of an efficient industrial process for methane upgrading have renewed interest in the oxidative coupling of methane (OCM) [1,2]. Since the unprecedented work of Keller and Bhasin in 1982 [3], OCM has been known as a promising route to convert methane directly into C_2 hydrocarbons (ethane and ethylene). However, the industrial deployment of the OCM route remains limited by the low C_2 yield resulting from inherent thermodynamic and kinetic limitations. Indeed, the high stability of methane and the faster formation of more thermodynamically stable CO_x compounds compared with that of C_2 hydrocarbons result in low, not economically competitive, C_2 yields [2,4,5]. Among hundreds of materials tested for OCM, Mn-Na_2WO_4/SiO_2 is considered as the state-of-the-art catalyst, exhibiting high stability (~500 h on stream) and C_2 yields (14–27%) [6,7]. However, for the OCM route to be economically viable, a single-pass C_2 yield of 30% and a C_2 selectivity of 90% are necessary [8,9].

Although a fundamental understanding of the Mn-Na_2WO_4/SiO_2 catalyst is crucial to design improved formulations, the literature remains unclear about the nature of the active sites and the mechanism for the selective activation of methane. On the one hand, several studies have ascribed the performance of the Mn-Na_2WO_4/SiO_2 catalyst for OCM to W^{6+} sites with distorted tetrahedral (T_d) oxygen coordination [10–12]. However, the proposed mechanisms for the selective activation of methane on these sites are inconsistent. Wu *et al.* suggested that the activation of methane occurs at lattice oxygen in the T_d-W^{6+} sites via a $W^{6+} \leftrightarrow W^{4+}$ redox cycle, where gas-phase oxygen completes the cycle [13]. Conversely, Jiang *et al.* proposed a $W^{6+} \leftrightarrow W^{5+}$ redox cycle along with a previous activation of gas-phase oxygen at the Mn^{3+} sites with octahedral (O_h) oxygen coordination [14]. The O_h-Mn^{3+} would act as oxygen storage-release sites via a $Mn^{2+} \leftrightarrow Mn^{3+}$ redox cycle, supplying activated oxygen species to the T_d-W^{6+} sites. On the other hand, Lunsford *et al.* proposed that the active sites are the Mn-O-

* Corresponding authors.
E-mail addresses: cbravo@peq.coppe.ufrj.br (C.A. Ortiz-Bravo), miguel.banares@csic.es (M.A. Bañares), toniolo@peq.coppe.ufrj.br (F.S. Toniolo).

https://doi.org/10.1016/j.jcat.2021.06.021
0021-9517/

Na sites instead of T_d-W^{6+} [15]. The activation of gas-phase oxygen would occur at the Mn-O-Na sites via dissociative adsorption, forming Mn-O-Na···O· sites, where methane then activates by cleaving C-H bond. However, W appears as a crucial performer: Elkins *et al.* recently showed the poor OCM performance of catalysts without W [16]. The absence of Na_2WO_4, Mn_2O_3, or α-cristobalite phases has been associated with worse OCM performances (*i.e.*, lower C_2 yields) [17–20]. The interplay between W, Mn and Na oxides on silica appears critical for this reaction.

Most OCM studies have explained catalytic performance with the crystalline phases observed by room temperature (RT) X-ray powder diffraction (XRD) [12–20]. For instance, the T_d-W^{6+} sites have been associated with the crystalline Na_2WO_4 phase with spinel structure (W^{6+} ions with T_d coordination) [10–13], whereas the O_h-Mn^{3+} sites have been associated with the crystalline Mn_2O_3 phase [14]. Thus, the crystalline Na_2WO_4 and Mn_2O_3 phases have been proposed as active phases for the OCM route. Moreover, the formation of the crystalline α-cristobalite phase from amorphous SiO_2 support during catalyst calcination has been deemed critical to stabilize distorted T_d-W^{6+} sites [16–18]. Other crystalline phases may also be present, depending on the catalyst synthesis method and precursors, such as $Na_2W_2O_7$, $MnWO_4$, quartz, and Mn_7SiO_2 [19–22].

The identification of active species by XRD is limited to the observation of crystalline phases with size larger than ca. 4 nm, being unable to report the potential presence of other structures such as (*i*) molecularly dispersed oxides, (*ii*) amorphous phases, (*iii*) nanocrystallites smaller than ca. 4 nm, or (*iv*) molten phases. Additionally, some crystalline phases with weak diffraction pattern intensities, such as Mn_2O_3, may be overwhelmed by the intense pattern of other crystalline phases, such as Mn_7SiO_{12}. Structure-activity/selectivity relationships based on *ex situ* XRD evidence may be inadequate because the crystalline phases identified at room temperature may not be the ones present during reaction. Actually, Mn-Na_2WO_4/SiO_2 is highly temperature-dependent: crystalline Na_2WO_4 and α-cristobalite phases undergo transitions during heating, as evidenced by differential scanning calorimetry (DSC) [23], high energy X-ray diffraction computed tomography (XRD-CT) [24,25] and Raman spectroscopy [21,26]. The XRD-CT studies fail to reveal the structure of the W sites at temperatures above 680 °C due to molten phases [25] and the X-ray absorption near edge structure (XANES) spectroscopy measurements were conducted in *ex situ* conditions [27]. Thus, determining the structure of the catalyst at temperatures where the OCM reactions can thermodynamically occur is critical to understand the nature of the species involved in the catalytic cycle.

While the Mn-Na_2WO_4/SiO_2 system is very dynamic, only a very recent OCM contribution provides complete information about its dynamic states present at relevant OCM temperatures (>700 °C) [21]. This work underscores the relevance of characterizing during activation and reaction to: (*i*) monitor the mean oxidation state and molecular geometry (distortion degree) of the W and Mn sites to reveal the potential existence of temperature-induced structural changes and (*ii*) evaluate the role of each catalyst component (silica support, W, Mn, and Na sites).

This work presents a systematic study to elucidate the electronic and molecular structure of the W and Mn sites on the Mn-Na_2WO_4/SiO_2 catalyst at relevant OCM reaction temperatures. For this purpose, the mean oxidation state, site symmetry, and distortion degree of the W and Mn sites on the conventional 2 wt% Mn-5 wt% Na_2WO_4/SiO_2 catalyst, and on Mn-free 5 wt% Na_2WO_4/SiO_2, and Mn- and Na-free 3.1 wt% WO_3/SiO_2 catalysts were determined via XRD and Raman and XANES spectroscopies at room temperature (RT) and *in situ* temperature-programmed oxidation (TPO). This study contributes to elucidating the nature of the active sites of this complex system.

2. Experimental

2.1. Catalyst synthesis

The conventional 2 wt% Mn-5 wt% Na_2WO_4/SiO_2 catalyst was synthesized via the incipient-wetness impregnation (IWI) method, in line with previous works discussing the nature of the active sites [6,10–16]. The catalyst precursors were those described elsewhere to minimize variations in the nature and dispersion of the supported phases [6,7,22]. The catalyst was synthesized by dissolving $Na_2WO_4{\cdot}2H_2O$ (Sigma-Aldrich, ACS reagent, ≥99%) and $Mn(NO_3)_2{\cdot}4H_2O$ (Sigma-Aldrich, ACS reagent, ≥97%) in a volume of deionized water equal to the pore volume (1.1 $cm^3{\cdot}g^{-1}$) of the silica support (Davisil Grade 646, 35–60 mesh, BET surface area = 401 $m^2{\cdot}g^{-1}$). The resulting solution was then added onto the silica under continuous stirring until the onset of incipient wetness. Finally, the sample was dried at 110 °C overnight and then calcined at 800 °C (1 °C·min^{-1}) for 5 h in a muffle furnace in static air. Additionally, Mn-free 5 wt% Na_2WO_4/SiO_2 and Mn- and Na-free 3.1 wt% WO_3/SiO_2 catalysts were synthesized by the same IWI method for comparison, mimicking W loading on the conventional Mn-Na_2WO_4/SiO_2 catalyst (~3.1 wt%). The Na_2WO_4/SiO_2 catalyst was synthesized using the same precursors as for the Mn-Na_2WO_4/SiO_2 catalyst, while $(NH_4)_6H_2W_{12}O_{40}{\cdot}nH_2O$, ammonium meta tungstate (AMT, Sigma-Aldrich, ACS reagent, ≥99.99%), was used as W precursor for the WO_3/SiO_2 catalyst, in agreement with Wu and Li [12].

2.2. Catalyst characterization

The chemical composition was measured via inductively coupled plasma optical emission spectroscopy (ICP-OES) using a PlasmaQuant PQ 9000 spectrometer from Analytik Jena. The specific surface area was calculated via nitrogen (N_2) physisorption experiments using an ASAP 2020 (Micromeritics) instrument at liquid N_2 temperature. The catalysts were degassed at 300 °C (10 °C·min^{-1}) for 24 h before the adsorption experiments. The specific surface areas were calculated using the multiple-point Brunauer-Emmett-Teller (BET) method to analyze the N_2 adsorption isotherms in a relative pressure range of 0.05–0.3.

X-ray powder diffraction (XRD) measurements were performed on a PANalytical X'Pert Pro diffractometer using CuK_α radiation (λ = 1.5406 Å) generated at 40 kV and 30 mA as the X-ray source. Crystalline phases were identified using the JCPDS (Joint Committee on Powder Diffraction Standards) database. RT-XRD patterns were collected in a Bragg angle (2θ) range of 5-90° with a step size of 0.02° and a counting time of 50 s per step. *In situ* TPO-XRD patterns were isothermally recorded in a high-temperature chamber (Anton Paar XRK900) every 50 °C from 50 °C to 800 °C during heating at 10 °C·min^{-1} under 100 $cm^3{\cdot}min^{-1}$ flow (molar O_2:Ar = 1:4). *In situ* measurement conditions were: 2θ range of 5-90°, step size of 0.05°, and a step counting time of 20 s.

In situ TPO-Raman spectra were taken with a confocal Renishaw inVia Qontor instrument equipped with a cooled CCD detector and three laser excitations (785, 514, and 405 nm). The 405 nm laser was chosen to minimize potential sample fluorescence and register Raman spectra at high temperatures. The spectral resolution was near 1.5 cm^{-1}, and the wavenumber calibration was checked using the silica standard band at 520.5 cm^{-1}. The laser was focused on the catalysts with a confocal microscope using an ultralong working distance x20 objective (Olympus LMPlanFL N 20X). Typically, ~0.05 g of each catalyst (180–250 μm) was loaded into a Linkam reaction cell that consists of a fixed-bed microreactor with a quartz window and O-ring seals, which was cooled by flowing water. The laser power on the catalyst was kept below 5 mW to prevent local

heating. For the *in situ* TPO-Raman study, each catalyst was initially dehydrated under 60 $cm^3 \cdot min^{-1}$ flow of O_2:Ar (molar ratio 1:2) at 200 °C (10 °C·min^{-1}) for 30 min and then cooled down to 25 °C. The catalyst was then heated to 800 °C (10 °C·min^{-1}) under the same oxidizing gas flow with simultaneous acquisition of Raman spectra (1 accumulation of 20 s) every 25 °C. The TPO-Raman study mimics the heating process typically used in the literature for testing the steady-state OCM performance of the conventional Mn-Na_2WO_4/SiO_2 catalyst [15,17,18]. The spectra were analyzed using PEAXACT software.

In situ TPO-XANES spectroscopy measurements at the W-L_3 and Mn-K edges were performed at the XAFS2 beamline at the Brazilian Synchrotron Light Laboratory (LNLS, Campinas, Brazil) [28], using ionization chambers to measure incident and transmitted beam intensities. A third ionization chamber was used for energy calibration purposes, measuring a reference (Ga foil or Mn foil, depending on the edge) simultaneously to the catalyst. For the *in situ* TPO-XANES studies each catalyst was loaded in a quartz capillary cell (I.D./O.D. = 1/1.01 mm) [29] and heated from 25 to 800 °C (10 °C·min^{-1}) under 10 $cm^3 \cdot min^{-1}$ of O_2:He (molar ratio 1:10). *In situ* Mn-K XANES spectra were isothermally collected in fluorescence mode at 25 and then every 100 °C from 100 °C up to 800 °C, while *in situ* W-L_3 XANES spectra were isothermally collected in transmission mode at 25, 700, 750, and 800 °C. For the latter, the catalyst was first flushed with He. Reference materials WO_3 (Sigma-Aldrich, 99.995%), Na_2WO_4 (Sigma-Aldrich, 99.995%), WO_2 (Sigma-Aldrich, 99.995%), MnO (Sigma-Aldrich, 99.9%), Mn_3O_4 (Sigma-Aldrich, >99%), Mn_2O_3 (Sigma-Aldrich, 99.99%), and MnO_2 (Sigma-Aldrich, >99%) were diluted with boron nitride to have a metal loading of 1–5 wt% and measured at ambient conditions. Data processing and analysis were conducted using Athena software [30].

2.3. Steady-state OCM catalytic tests

Steady-state reaction studies were performed in a fixed-bed catalytic reactor. Typically, 0.1 g of each catalyst (180–250 μm) was diluted with 0.4 g of carborundum (SiC, 180–250 μm, Sigma-Aldrich) and supported in a quartz U-shape reactor tube (I.D. = 10 mm) between two pieces of quartz wool. The reactor was placed into an electric furnace, and the reaction temperature was measured and controlled using a thermocouple attached to the outside wall of the reactor in a position corresponding to the middle of the catalyst bed length. Both inlet and outlet gas lines were heated at 120 °C to prevent condensation. Gaseous products were analyzed using an on-line gas chromatograph (Shimadzu GC-2014) equipped with two channels of separation and detection: (*i*) a polar carboxen 1010 PLOT capillary column (30 m × 0.32 mm #35789-02A) coupled with thermal conductivity (TCD) and flame ionization (FID) detectors; and (*ii*) a CP-Molsieve 5A column (25 m × 0.53 mm #CP7538) coupled with a TCD detector. Before starting the reaction, each catalyst was heated up to reaction temperature under 60 $cm^3 \cdot min^{-1}$ of a mixture O_2:He:N_2 (molar ratio 2:3:1). Such is the heating process typically used before testing the OCM activity of the Mn-Na_2WO_4/SiO_2 catalyst because increasing temperature under oxidizing conditions has been proposed to enhance the C_2 selectivity [15,17,18,31]. The reaction started by feeding 73 $cm^3 \cdot min^{-1}$ of a mixture CH_4:O_2:He:N_2 (molar ratio 2:1:1.5:0.5) to the reactor. N_2 was used as a GC internal standard. The OCM catalytic activity was measured at 650, 700, 750, and 800 °C after 30 min to allow the reaction to reach the steady-state at each temperature. The water produced during the catalytic test was separated from the gaseous products before entering the GC using a condenser trap cooled by a cryostat. The conversion of methane (X_{CH4}) and the selectivity to C_2 hydrocarbons (S_{C2}) were calculated from the mole number of the detected compounds, derived from a carbon balance of the system as follows:

$$X_{CH_4} = \frac{(CH_4)_{in} - (CH_4)_{out}}{(CH_4)_{in}} \cdot 100 \quad (1)$$

$$S_{C_2} = \frac{2\ (C_2H_4 + C_2H_6)}{2\ (C_2H_4 + C_2H_6) + CO_2 + CO} \cdot 100 \quad (2)$$

Replicate experiments involving reloading catalyst into the reactor resulted in standard deviations near 0.9% for both X_{CH4} and S_{C2}. The turnover frequency (TOF) was calculated for each catalyst at 650, 700, 750, and 800 °C as the number of reacted CH_4 moles per mol of W in the reactor per second, as described in the Supporting Information. It was assumed that all W atoms of the catalyst, calculated from the W concentration measured by ICP-OES analysis (Table S1), interact with methane.

3. Results and discussion

3.1. Catalyst characterization

Table S1 (see Supporting Information) presents the chemical composition and specific surface areas of the synthesized WO_3/SiO_2, Na_2WO_4/SiO_2, and Mn-Na_2WO_4/SiO_2 catalysts. W loadings (3.2–3.4 wt%) agreed well with the theoretical value (3.1 wt%) of the conventional 2 wt% Mn-5 wt% Na_2WO_4/SiO_2 catalyst. Figs. S1-S3 show the N_2 adsorption–desorption isotherms. The catalysts exhibited a significantly lower specific surface area than the amorphous silica used as support (401 $m^2 \cdot g^{-1}$). This can be attributed to the partial plugging of the silica pores by the supported oxides, limiting the accessibility of N_2 molecules, and to the partial collapse of the silica porous structure at the high calcination temperature employed (800 °C). The Na_2WO_4/SiO_2 and Mn-Na_2WO_4/SiO_2 catalysts (14 and 11 $m^2 \cdot g_{cat}^{-1}$, respectively) exhibited a higher surface area decrease than the WO_3/SiO_2 catalyst (150 $m^2 \cdot g_{cat}^{-1}$) due to the presence of Na^+, which tends to collapse the porous silica structure during calcination [18]. Na^+ diffuses within the silica framework, cleaves the Si-O-Si bridges, and forms non-bridging oxygen bonds typical of crystalline silica phases [32]. The Na-induced silica crystallization with simultaneous specific surface area decrease has been extensively reported for the Mn-Na_2WO_4/SiO_2 catalyst [15,16,20,22,32–37].

XRD analysis. The qualitative phase identification of the synthesized catalysts was performed via XRD analysis at room temperature (RT) and temperature-programmed oxidation (TPO). Fig. 1 shows the RT-XRD patterns of the WO_3/SiO_2, Na_2WO_4/SiO_2, and Mn-Na_2WO_4/SiO_2 catalysts.

The WO_3/SiO_2 catalyst maintains the amorphous silica phase of the support, exhibiting only diffraction peaks related to the crystalline monoclinic (space group $P2_1/n$) γ-WO_3 phase (Fig. 1a). The crystalline WO_3 nanoparticles (NPs) are formed upon calcination because its surface density, 0.7 W-atoms·nm^{-2}, is beyond the W dispersion limit loading ("monolayer" coverage, ca. 0.5 W-atoms·nm^{-2}) [38]. XRD is not sensitive to report about molecularly dispersed WO_x species. The synthesized catalysts containing Na (*i.e.*, Na_2WO_4/SiO_2 and Mn-Na_2WO_4/SiO_2) exhibit diffraction peaks related to the cubic (Fd-3 m) Na_2WO_4 phase and two crystalline silica phases: tetragonal ($P4_12_12$) α-cristobalite and orthorhombic ($I2_12_12_1$) tridymite. Both silica phases were formed by the Na-induced crystallization of the amorphous silica support during the catalyst calcination, in agreement with the literature [16–18]. Additionally, the Mn-Na_2WO_4/SiO_2 catalyst exhibits a low-intensity diffraction peak near 2θ = 33.02° attributable to either Mn_2O_3 (bixbyite) or Mn_7SiO_{12} (braunite). Discriminating between these phases is challenging because both exhibit their highest

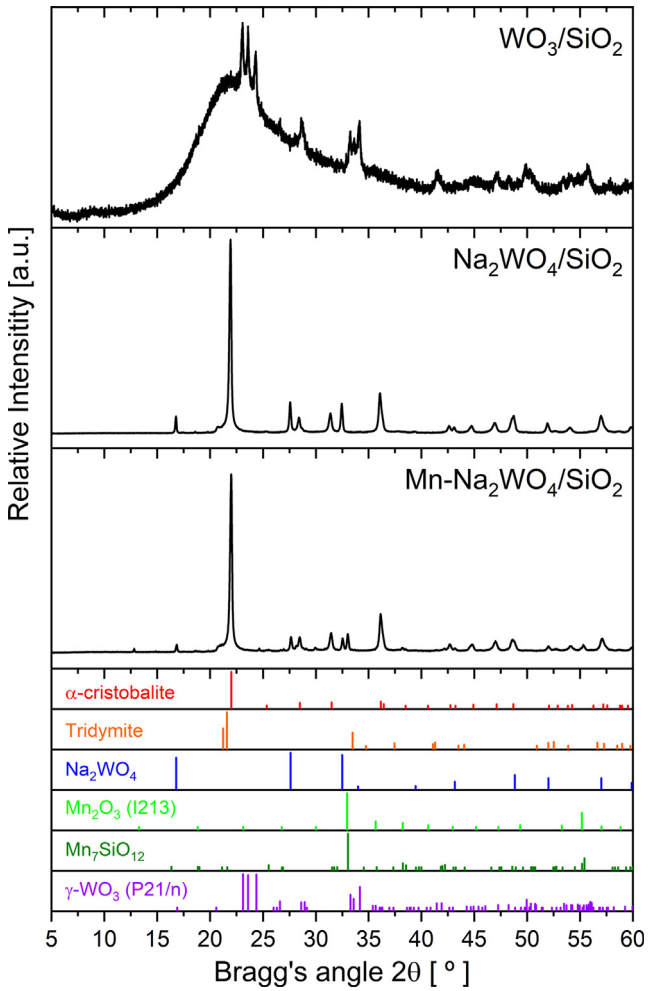

Fig. 1. RT-XRD patterns of the WO_3/SiO_2, Na_2WO_4/SiO_2, and Mn-Na_2WO_4/SiO_2 catalysts. Diffraction patterns of the identified crystalline phases are also included: α-cristobalite [ICSD 030269] (red tick marks), tridymite [ICSD 038252] (orange tick marks), Na_2WO_4 [ICSD 028474] (blue tick marks), Mn_2O_3 [ICSD 033647] (light green tick marks), Mn_7SiO_{12} [ICSD 012123] (dark green tick marks), and γ-WO_3 [ICSD 016080] (purple tick marks). (For interpretation of the references to colour in this figure legend, the reader is referred to the web version of this article.)

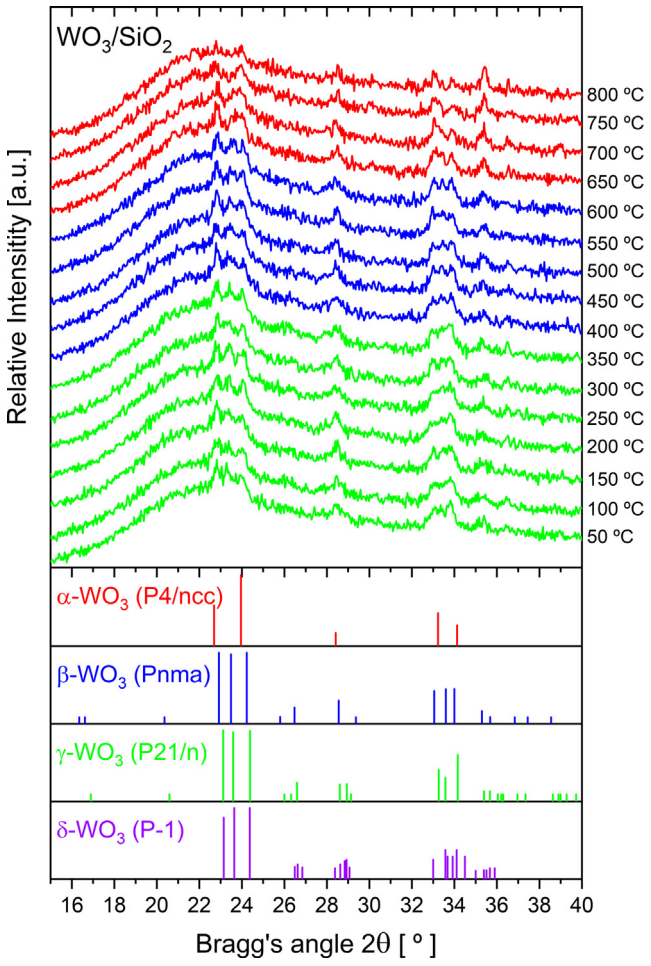

Fig. 2. *In situ* TPO-XRD patterns of the WO_3/SiO_2 catalyst recorded between 50 °C and 800 °C (10 °C·min^{-1}) under O_2:Ar = 1:4 (100 cm^3·min^{-1}). Diffraction patterns of some WO_3 polymorphs are also included: tetragonal (P4/ncc) α-WO_3 [ICSD 027961] (red tick marks), orthorhombic (Pnma) β-WO_3 [ICSD 000836] (blue tick marks), monoclinic (P21/n) γ-WO_3 [ICSD 016080] (green tick marks), and triclinic (P-1) δ-WO_3 [ICSD 080055] (purple tick marks). (For interpretation of the references to colour in this figure legend, the reader is referred to the web version of this article.)

intensity peak very close. The (222) reflection of Mn_2O_3 is at 2θ = 32.94°, and the (224) reflection of Mn_7SiO_{12} is at 2θ = 33.04°. The peak was finally attributed to the crystalline Mn_2O_3 phase, based on its Raman spectrum (Fig. 4c).

The thermal stability of the crystalline phases identified at room temperature was monitored by TPO-XRD analysis. Fig. 2 shows the *in situ* TPO-XRD patterns of the WO_3/SiO_2 catalyst and the diffraction patterns of some WO_3 polymorphs that can form upon heating. The qualitative phase identification is challenging due to the low crystallite size of the WO_3 NPs (loading slightly above "monolayer" coverage) and the faster step counting time compared with the RT-XRD measurements. However, the crystalline WO_3 phase can be monitored by following two groups of the main diffraction peaks in the 22° < 2θ < 25° and 32° < 2θ < 34° windows. Upon heating, the diffractograms hardly change until 400 °C, when the three diffraction peaks at 32° < 2θ < 34° exhibit similar intensity, suggesting the presence of the orthorhombic (Pnma) β-WO_3 phase. A distinct diffraction pattern characterized by two peaks at 2θ = 22.88° and 23.87°, and 2θ = 33.23° and 33.84° is observed at 650 °C, suggesting the presence of the tetragonal (P4/ncc) α-WO_3 phase, which remains stable until 800 °C. These temperature-induced (monoclinic) γ ↔ (orthorhombic) β ↔ (tetragonal) α-WO_3 phase transitions are reversible [39,40].

Fig. 3 shows the *in situ* TPO-XRD patterns of the Na_2WO_4/SiO_2 and Mn-Na_2WO_4/SiO_2 catalysts. While the diffraction peaks of the tridymite phase of the support do not evolve during the heating up to 800 °C, the α-cristobalite transforms into the β-cristobalite phase. The (101) (2θ = 22.02°), (111) (2θ = 28.49°), (102) (2θ = 31.49°), and (200) (2θ = 36.16°) diffraction peaks of the tetragonal α-cristobalite phase vanish, while the (111) (2θ = 21.46°) and (220) (2θ = 35.40°) peaks of the cubic (Fd-3 m) β-cristobalite phase appear and remain stable in diffractograms obtained above 200 °C. On the other hand, the diffraction peaks of the cubic Na_2WO_4 phase disappear at 600 °C, while the diffraction peaks of the lower symmetry orthorhombic Na_2WO_4 phase arise and remain present until 650 °C. Further heating leads to the complete disappearance of Na_2WO_4 reflections, suggesting its melting. DSC and Raman spectroscopy results reported in the literature show that these transitions are reversible [21,23], which emphasizes the importance of *in situ* studies, as fresh or spent catalysts at room temperature would not provide relevant information about the catalyst structure during OCM.

The *in situ* TPO-XRD patterns of the Mn-Na_2WO_4/SiO_2 catalyst show that the crystalline Mn_2O_3 phase remains present up to, at

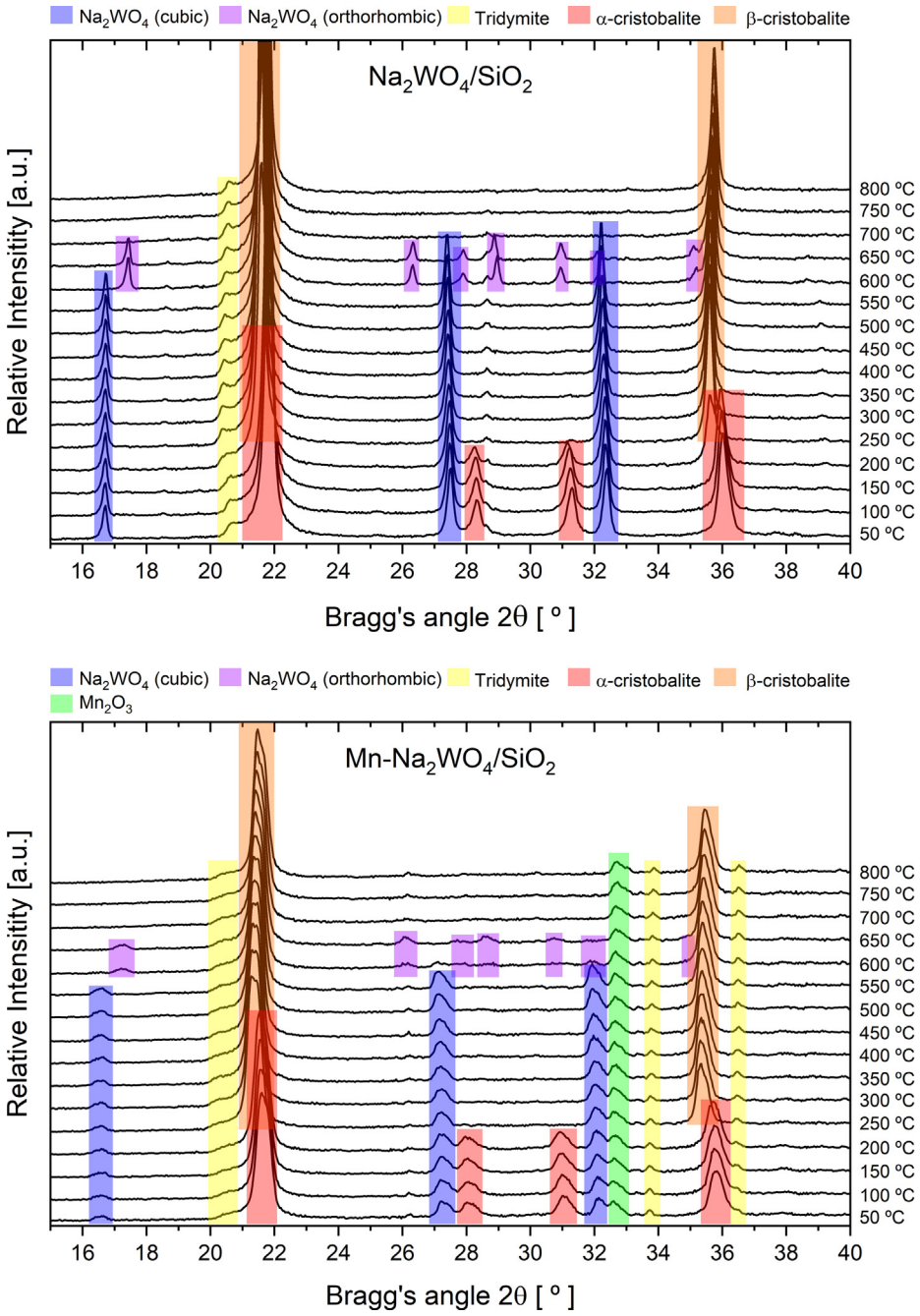

Fig. 3. *In situ* TPO-XRD patterns of the Na_2WO_4/SiO_2 and Mn-Na_2WO_4/SiO_2 catalysts recorded between 50 °C and 800 °C (10 °C·min^{-1}) under O_2:Ar = 1:4 (100 cm^3·min^{-1}). Diffraction patterns of the crystalline phases identified at high temperatures are also included: orthorhombic (***Pnam***) Na_2WO_4 [ICDD 00–020-1163] (purple box) and cubic (***Fd*-3 *m***) β-cristobalite [ICSD 034924] (orange box). (For interpretation of the references to colour in this figure legend, the reader is referred to the web version of this article.)

least, 800 °C. The structure of W species above 700 °C cannot be determined by XRD due to Na_2WO_4 melting; fortunately, such phases can be monitored with Raman spectroscopy.

***In situ* TPO-Raman**. Fig. 4 shows the *in situ* TPO-Raman spectra of the dehydrated WO_3/SiO_2, Na_2WO_4/SiO_2, and Mn-Na_2WO_4/SiO_2 catalysts recorded between 25 °C (RT) and 800 °C (10 °C·min^{-1}). The spectra were normalized against the Rayleigh band at 0 cm^{-1} [41].

At room temperature, the dehydrated WO_3/SiO_2 catalyst exhibits Raman bands typically ascribed to the crystalline WO_3, in agreement with RT-XRD (Fig. 4a, left) [42]. The crystalline WO_3 phase has three major Raman bands at 805, 713, and 265 cm^{-1}, corresponding to the symmetrical (ν_s) and asymmetrical (ν_{as}) stretching modes, and the bending (δ_s) mode of the bridging W-O-W bond, respectively [43]. The surface density of W atoms on the WO_3/SiO_2 catalyst (~0.7 W-atoms·nm^{-2}) is above de dispersion limit surface coverage. Thus, the presence of the dispersed WO_x phase is unlikely, as confirmed by Raman spectroscopy (see Fig. S4).

The dehydrated Na_2WO_4/SiO_2 and Mn-Na_2WO_4/SiO_2 catalysts exhibit Raman bands related to the crystalline α-cristobalite and cubic Na_2WO_4 phases (Fig. 4b-c, left). The crystalline α-cristobalite phase gives rise to Raman bands at 1075, 785, 415, and 228 cm^{-1} [44]. The crystalline Na_2WO_4 phase exhibits Raman bands at 926, 810, and 309 cm^{-1}, corresponding to the symmetrical (ν_s) and asymmetrical (ν_{as}) stretching modes, and the bending

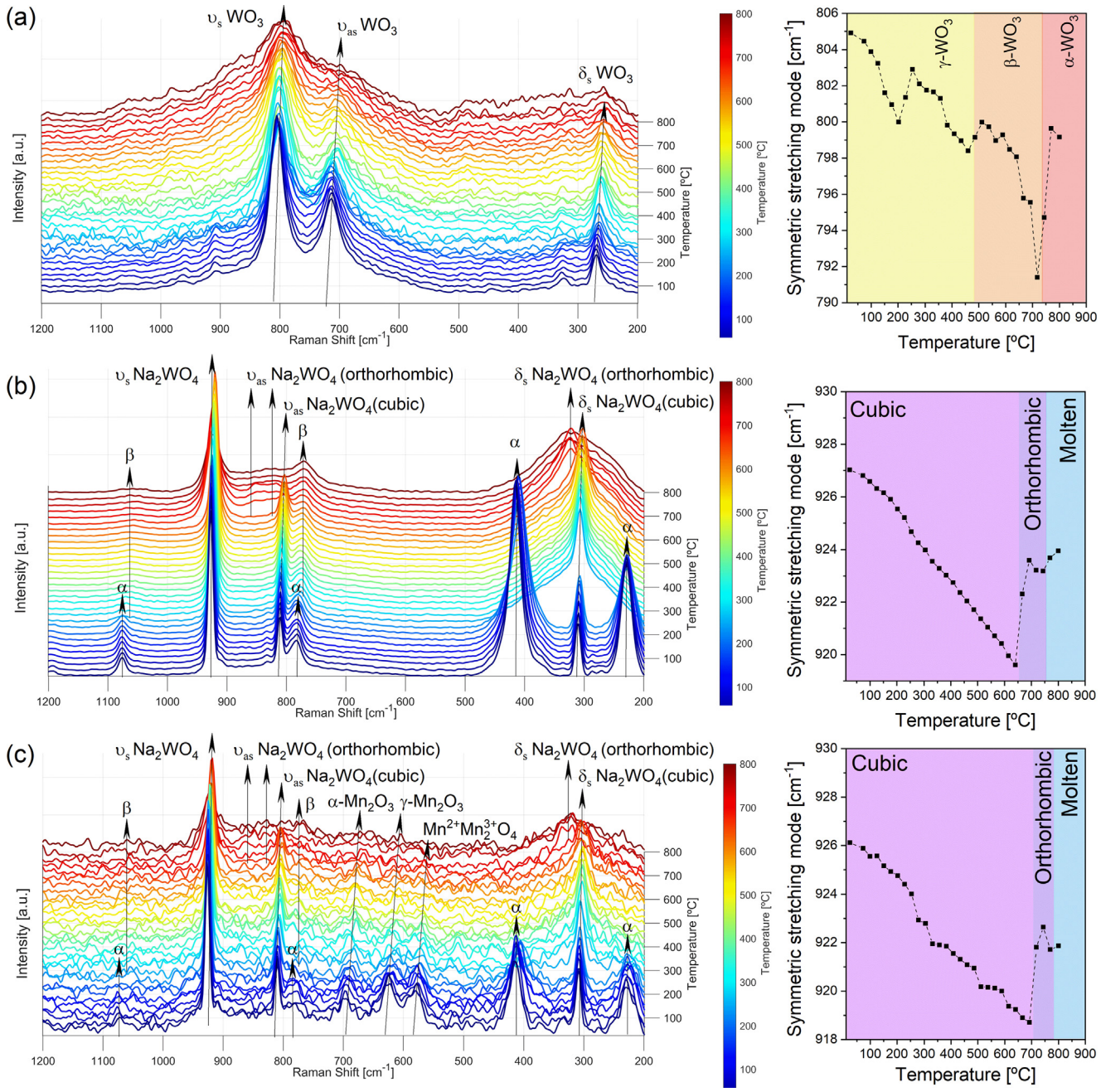

Fig. 4. *In situ* TPO-Raman spectra (excitation at 405 nm, normalization against Rayleigh band at 0 cm^{-1}), left, and position of the ν_s vibration band (symmetric stretching mode) of tungsten species as a function of temperature, right, of the dehydrated: (a) WO_3/SiO_2, (b) Na_2WO_4/SiO_2, and (c) Mn-Na_2WO_4/SiO_2 catalysts recorded between 25 °C and 800 °C (10 °C·min^{-1}) under O_2:Ar = 1:2 (60 cm^3·min^{-1}).

(δ_s) mode of the W-O bond, respectively [45]. Dispersed WO_x species on the dehydrated Na_2WO_4/SiO_2 and Mn-Na_2WO_4/SiO_2 catalysts were not observed, in agreement with Werny *et al.* [21]. The formation of Mn_7SiO_{12} (Braunite) phase can be ruled out because of the absence of Raman bands in the 470–550 cm^{-1} range [46], which underpins the decision of assigning the low-intensity diffraction peak near 2θ = 33.02° of Fig. 1 to Mn_2O_3 (Bixbyite). Thus, the Raman bands at 698, 624, and 564 cm^{-1} are associated with the crystalline α-Mn_2O_3, γ-Mn_2O_3, and hausmanite $Mn^{2+}Mn_2^{3+}O_4$ phases, respectively [47,48].

XRD and Raman uncover W sites with different environments; the W sites are octahedrally coordinated in the WO_3/SiO_2 (O_h-W^{6+} sites in the WO_3 phase) and tetrahedrally coordinated in the Na_2WO_4/SiO_2 and Mn-Na_2WO_4/SiO_2 (T_d-W^{6+} sites in the Na_2WO_4 phase) [43,49]. The position of the most intense Raman band denotes the highest bond order (shortest W-O bond) of tungsten species [49]. Thus, the crystalline WO_3 phase (O_h-W^{6+} sites) exhibits the most intense Raman band, related to the symmetrical (ν_s) stretching mode, at lower wavenumber (805 cm^{-1}) than the crystalline Na_2WO_4 phase (T_d-W^{6+} sites) (ca. 926 cm^{-1}) due to the lower bond order of the former [43,49]. The different symmetry of the W sites in the synthesized catalysts is due to the presence of Na^+ cations [12]. The resulting catalysts exhibited Raman bands related to T_d-W^{6+} sites in the crystalline Na_2WO_4 phase, in line with XRD results and a recent study by Kiani *et al.* on the molecular and electronic structure of the W sites on model SiO_2-supported

Na-promoted tungsten oxide catalysts [26]: the W sites exhibited T_d symmetry in the dispersed Na-WO_4 and the crystalline Na_2WO_4 phases.

Temperature-induced structural modifications of the W sites can be followed by measuring the position of the ν_s vibration band because changes in the oxidation state and/or distortion degree impose variations on the bond order of tungsten species [49]. Fig. 4, right, shows the position of the ν_s vibration band of the crystalline WO_3 phase on the WO_3/SiO_2 catalyst (a) and of the crystalline Na_2WO_4 phase on the Na_2WO_4/SiO_2 (b) and Mn-Na_2WO_4/SiO_2 (c) catalysts as a function of temperature in the TPO-Raman study. The ν_s vibration band in the WO_3/SiO_2 catalyst red shifts with increasing temperature but undergoes two sharp blue shifts near 450 and 700 °C, suggesting the temperature-induced γ (monoclinic) → β (orthorhombic) → α-WO_3 (tetragonal) phase transitions, respectively (Fig. 4a, right). The overall red shift indicates a decrease in the bond order of the O_h-W^{6+} sites with increasing temperature. This is due to an elongation of the W-O bond. The sequential γ.→.β→.α-WO_3 phase transitions are thus corroborated by following the δ_s vibration band, which monotonically red shifts with temperature up to ~700.°C. The presence of the crystalline α-WO_3 phase at 800 °C is confirmed by the broadening of the ν_{as} vibration band (Fig. 4a, left) [42].

The TPO-Raman study of the dehydrated Na_2WO_4/SiO_2 catalyst monitors the α → β-cristobalite and cubic → orthorhombic → molten Na_2WO_4 transitions observed via TPO-XRD analysis elsewhere. Regarding the α → β-cristobalite phase transition, the band at 1075 cm^{-1} broadens, weakens, and slightly redshifts to 1073 cm^{-1}, the band at 785 cm^{-1} slightly red shifts to 782 cm^{-1}, and the bands at 415 and 228 cm^{-1} vanish above 250 °C. Thus, the crystalline β-cristobalite phase gives rise to Raman bands at 1073, 782, and 292 cm^{-1}, which remain constant until 800 °C (Fig. 4b, left) [44]. Note that the δ_s vibration band of the cubic Na_2WO_4 phase (~309 cm^{-1}) overlaps the β-cristobalite band at 292 cm^{-1} above 250 °C [26].

Concerning the Na_2WO_4 phase transitions: the ν_s vibration of the Na_2WO_4/SiO_2 catalyst red shifts with increasing temperature but undergoes two sharp blue shifts near 650 and 750 °C, suggesting successive temperature-induced cubic → orthorhombic → molten Na_2WO_4 transitions. The cubic → orthorhombic Na_2WO_4 transition is also corroborated by the blue shift of the δ_s vibration from 309 to 319 cm^{-1} and the split of the ν_{as} vibration band at 810 cm^{-1} into two smaller ones at 847 and 820 cm^{-1} (Fig. 4b, left) (for a more detailed view see Fig. S5) [50,51]. The bands at 923, 847, 820, and 319 cm^{-1} related to the orthorhombic Na_2WO_4 phase loose intensity with a further temperature increase and the ν_s band blue shifts, suggesting the melting of the Na_2WO_4 phase near 750 °C (Fig. 4b, right).

The temperature-induced γ → β → α-WO_3, α → β-cristobalite, and cubic → orthorhombic → molten Na_2WO_4 transitions observed by the TPO-Raman study take place at higher temperatures than those observed by TPO-XRD analysis. This may be due to the different heating ramps imposed by the equipments. Note that, for instance, the complete formation of the orthorhombic Na_2WO_4 phase requires some 4 min or 40 °C in a continuous 10 °C·min^{-1} heating ramp under oxidizing conditions to occur, according to DSC measurements [21].

Monitoring the structure of the W sites on the conventional Mn-Na_2WO_4/SiO_2 catalyst during the heating via Raman spectroscopy is challenging due to the broadness of the bands (Fig. 4c, left). The UV–vis spectra of the three catalysts (Fig. S6) show that the addition of Mn increased the absorption (broad band near 400 nm). The sequential cubic → orthorhombic → molten Na_2WO_4 transition in the Na_2WO_4/SiO_2 catalyst is also apparent in the dehydrated Mn-Na_2WO_4/SiO_2 catalyst. The ν_s vibration shows an overall red shift with increasing temperature up to near 700 °C, and then, two sudden blue shifts above 700 and 780 °C, associated with the sequential cubic → orthorhombic → molten Na_2WO_4 transitions (Fig. 4c, right). These transitions take place at higher temperatures than on the Na_2WO_4/SiO_2 catalyst (above 650 and 750 °C, respectively), suggesting the relevance of Mn on the thermal evolution of W sites. The α → β-cristobalite phase transition and the presence of the crystalline Mn_2O_3 phase on the dehydrated Mn-Na_2WO_4/SiO_2 catalyst throughout the heating had to be elucidated via chemometric component analysis using indirect hard modeling method with PEAXACT software (Fig. S7). The α → β-cristobalite phase transition occurs near 250 °C, as in the Na_2WO_4/SiO_2 catalyst, while the crystalline Mn_2O_3 phase remains stable up to 800 °C, in agreement with the TPO-XRD findings elsewhere.

Although the cubic → orthorhombic → molten Na_2WO_4 phase transitions have already been reported in the literature, understanding the structure of the W sites in the molten Na_2WO_4 phase is crucial because this phase is present at temperatures where the OCM reactions are thermodynamically relevant (>700 °C).

***In situ* TPO-XANES Spectroscopy**. The temperature-induced electronic and structural changes of the W and Mn sites were also studied via *in situ* TPO-XANES spectroscopy to complete the characterization and elucidate if the shift of the ν_s vibration band observed in the TPO-Raman study is due to a change in the oxidation state, the distortion degree of the W sites, or both. Fig. 5

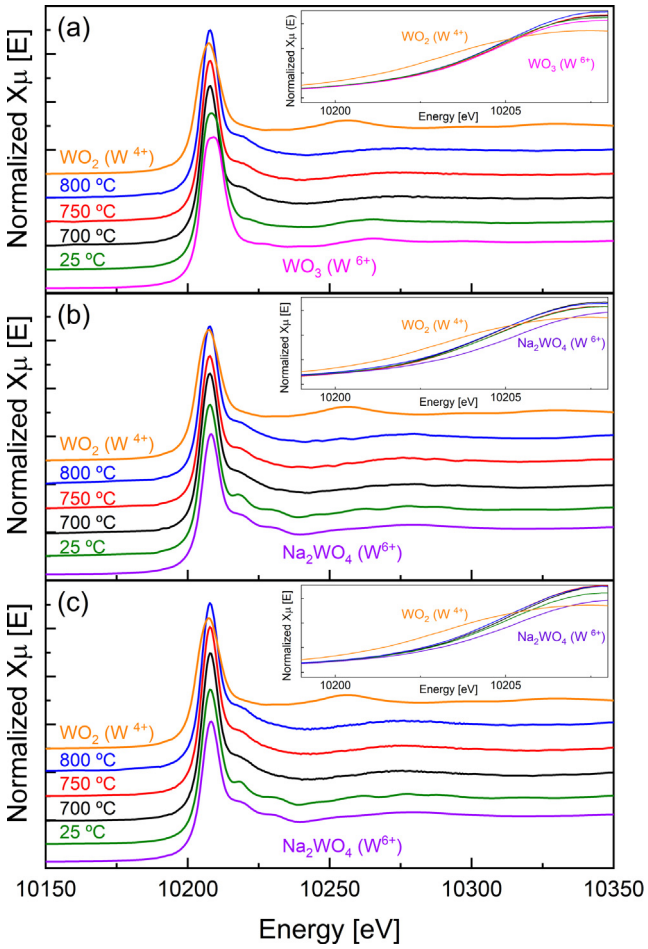

Fig. 5. *In situ* XANES spectra at the W-L_3 edge of the: (a) WO_3/SiO_2, (b) Na_2WO_4/SiO_2, and (c) Mn-Na_2WO_4/SiO_2 catalysts recorded at 25, 700, 750 and 800 °C under O_2:He = 1:10 (10 $cm^3 \cdot min^{-1}$). Insets show a detailed view of the edge region. Spectra of the reference materials WO_3 (W^{6+}), Na_2WO_4 (W^{6+}), and WO_2 (W^{4+}) are included in the figure.

depicts the *in situ* XANES spectra at the W-L_3 edge of the bulk WO_3, Na_2WO_4, and WO_2 reference materials recorded at 25 °C and the WO_3/SiO_2, Na_2WO_4/SiO_2, and Mn-Na_2WO_4/SiO_2 catalysts recorded at 25, 700, 750, and 800 °C. Insets in the upper right-hand corner show a more detailed view of the edge region.

The electron transition from the $2p_{3/2}$ state to a vacant 5*d* state appears as an intense dipole-allowed peak in the absorbance curve, known as the "white line" [52]. To calculate the mean oxidation state of the W atoms, the W-L_3 edge position (*i.e.*, the absorption threshold) for the bulk WO_3, Na_2WO_4, and WO_2 reference materials and the WO_3/SiO_2, Na_2WO_4/SiO_2, and Mn-Na_2WO_4/SiO_2 catalysts was determined by using the intersection with the energy axis of the second derivative with respect to the energy of the normalized XANES curve. Certainly, the energy shift on the W-L_3 edge position in tungsten species is due to differences in the mean oxidation state of the W atoms [53,54].

The W-L_3 edge position measured for the bulk WO_3, Na_2WO_4, and WO_2 reference materials was 10205.3, 10205.6, and 10203.3 eV, respectively. Thus, the W-L_3 edge position depends not only on the mean oxidation state, WO_3 (W^{6+}) *vs.* WO_2 (W^{4+}), but also on the local structure of the W atom, WO_3 (O_h-W^{6+}) *vs.* Na_2WO_4 (T_d-W^{6+}), in agreement with the literature [52]. Therefore, to estimate the mean oxidation state of the W sites at each temperature, the W-L_3 edge position measured for the WO_3/SiO_2 catalyst was interpolated to a straight line between the edge values recorded for the bulk WO_3 (O_h-W^{6+}) and WO_2 (O_h-W^{4+}) reference materials, as shown in Fig. S8a, and that of the Na_2WO_4/SiO_2 and Mn-Na_2WO_4/SiO_2 catalysts was calculated using the bulk Na_2WO_4 (T_d-W^{6+}) reference material instead of the WO_3 (O_h-W^{6+}), Fig. S8b. Table 1 summarizes the edge position and mean oxidation state of the W sites on each catalyst at 25, 700, 750, and 800 °C.

All synthesized catalysts exhibit a lower W-L_3 edge position than the bulk WO_3 and Na_2WO_4 reference materials at room temperature, suggesting that the mean oxidation state of the W sites is lower than 6+, in line with the known chemistry of WO_3 [55]: its polymorphic nature and tendency to form Magnéli phases, which stabilize cations with oxidation states below W^{6+}. Thus, the WO_3/SiO_2, Na_2WO_4/SiO_2, and Mn-Na_2WO_4/SiO_2 catalysts have W^{6+} sites with some electron polarons (*i.e.*, W^{5+} at a W^{6+} site). The formation of oxygen-deficient W oxides by single self-trapped electron polarons in small amounts is expected in the crystalline WO_3 and Na_2WO_4 phases [56–59]. On the other hand, the increasing temperature under oxidizing conditions did not shift the W-L_3 edge position out of the error in the energy resolution for any catalyst. Thus, the electronic state of the W sites remains as W^{5+}-W^{6+} ~~sites~~ at relevant OCM temperatures. To summarize, the *in situ* TPO-XANES spectra indicate that the temperature-induced ν_s vibration band shift observed in the TPO-Raman study is related to a variation in the distortion degree of the W sites rather than a variation in the oxidation state.

The intensity and shape of the white line also provide information about the oxidation state and symmetry of the W sites. On the one hand, the intensity is associated with the density of unoccupied states, and therefore with the oxidation state. Thus, the white line intensity of the WO_3 (W^{6+}) is higher than that of the WO_2 (W^{4+}) [52]. However, the higher intensity evidenced for the synthesized catalysts compared with the bulk WO_3 and Na_2WO_4 reference materials (even at room temperature) cannot be associated with a higher oxidation state of the W sites, since the edge position remained unchanged. This effect is actually related to the interaction of the WO_3 and Na_2WO_4 NPs with the support, in agreement with the literature [60]. Garcia-Lopez *et al.* recently observed that the white line intensity of the silica-supported Keggin $[PW_{12}O_{40}]^{3-}$ and Wells – Dawson $[P_2W_{18}O_{62}]^{6-}$ heteropolyanions were higher than that of the unsupported heteropolyanions [60]. On the other hand, the white line shape depends on the symmetry and distortion of the W atoms [61,62]. Although both WO_3 and Na_2WO_4 reference materials have the same oxidation state (W^{6+}, d^0), they present different white line shapes. The crystalline WO_3 phase (O_h-W) exhibits a broad peak with an indistinct top (Fig. 5a), whereas the Na_2WO_4 (T_d-W) exhibits a sharper, more asymmetrical peak (Fig. 5b-c). These differences are due to the splitting of the W 5*d* state by the ligand field [61,62]. Thus, the broad white line of the O_h-W sites consists of two peaks related to the t_{2g} (d_{xy}, d_{yz}, and d_{zx}) and e_g ($d^2_{x^2-y^2}$ and $d^2_{z^2}$) orbitals, whereas the narrow white line of the T_d-W sites is due to a smaller splitting of the W 5*d* state and consists of two peaks related to the *e* and t_g orbitals [60–63].

To analyze the temperature-induced changes in the distortion degree of the W sites, the white line shape of the synthesized catalysts at each temperature was interpreted by considering the final state of the 5*d* orbitals following a methodology proposed by Yamazoe *et al.* [61]. The white line was deconvoluted by representing each electron transition to a vacant 5*d* split orbital with a Lorentz function and the vacuum level with an arctangent function. Two Lorentz peaks, at lower and higher energy, related to the t_{2g} and e_g orbitals for the O_h-W^{6+} sites or the *e* and t_g orbitals for the T_d-W^{6+} sites, were adjusted. The two peaks in the second derivative of the bulk WO_3 and Na_2WO_4 reference materials were considered as the input center values for the Lorentz peaks in catalysts with O_h-W^{6+} and T_d-W^{6+} sites, respectively (Fig. S9). The peak ratio of t_{2g}/e_g = 3/2 and e/t_g = 2/3 were considered as constraints. Irrespective of the temperature, because the oxidation state of the samples did not change, the arctangent functions adjusted for the bulk WO_3 and Na_2WO_4 reference materials were used to deconvolute the white line of the WO_3/SiO_2 catalyst and of the Na_2WO_4 and Mn-Na_2WO_4/SiO_2 catalysts, respectively. The energy gap between both peak centers reflects the 5*d* state splitting. This analysis was similar to that carried out in previous works reported in the literature [60–64]. Fig. S10 shows a representative example of the fit performed for the bulk WO_3 reference material. The results of all the spectra deconvolutions are reported in Table S3, and Fig. 6 contrasts the measured energy gap values with the phases identified by TPO-XRD at each temperature range.

The energy gap for the bulk WO_3 and Na_2WO_4 reference materials at room temperature is 4.4 and 1.6 eV, respectively (Table S3), in agreement with the values reported in the literature (4.5 and 1.7 eV, respectively) [61,64]. Thus, the O_h-W sites exhibit a larger splitting of the W 5*d* state than the T_d-W sites, as discussed before.

Table 1
W-L_3 edge position according to the zero-crossing of the second derivative and mean W oxidation state obtained by interpolation. Errors in mean oxidation state derived from incertitudes on edge energy determinations.

Temperature [°C]	WO_3/SiO_2		Na_2WO_4/SiO_2		Mn-Na_2WO_4/SiO_2	
	Edge position [eV]	Mean W oxidation state	Edge position [eV]	Mean W oxidation state	Edge position [eV]	Mean W oxidation state
25	10205.0	5.7 ± 0.1	10205.1	5.6 ± 0.1	10205.1	5.6 ± 0.1
700	10205.0	5.7 ± 0.1	10205.0	5.5 ± 0.1	10205.1	5.6 ± 0.1
750	10205.1	5.8 ± 0.1	10205.0	5.5 ± 0.1	10205.1	5.6 ± 0.1
800	10205.0	5.7 ± 0.1	10205.0	5.5 ± 0.1	10205.0	5.5 ± 0.1

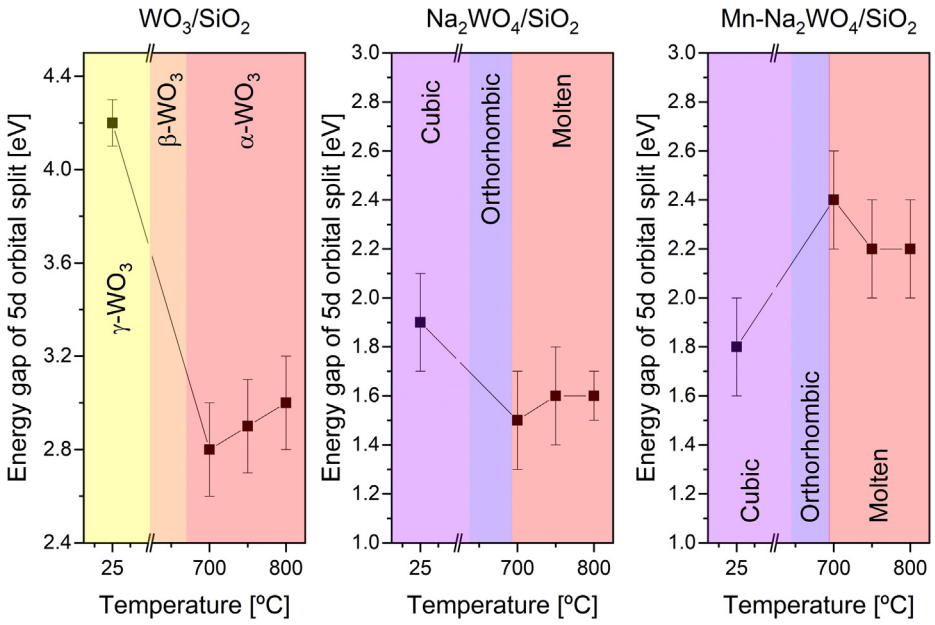

Fig. 6. Energy gap of the 5d split orbitals at the W-L_3 edge (XANES) as a function of temperature and in relation to the observed ~~crystalline~~ phases for the WO_3/SiO_2, Na_2WO_4/SiO_2, and Mn-Na_2WO_4/SiO_2 catalysts.

Regarding the general decrease of this parameter observed with temperature, some works attribute the decrease in the energy gap to an increase in the distortion degree of the O_h– and T_d-W sites [60,61]. The distortion of regular O_h symmetrical units solves the degeneracy of 5*d* orbitals and results in smaller splitting of the 5*d* orbitals [62]. In the WO_3/SiO_2 catalyst, the temperature-induced phase transition of the crystalline WO_3 phase observed in our TPO-Raman study suggests changes in the distortion degree of the O_h-W sites. The transition from the highly distorted monoclinic γ-WO_3 phase at room temperature to the ideal undistorted cubic WO_3 phase at very high temperatures (~1500 °C) in the sequence γ (monoclinic) → β (orthorhombic) → α (tetragonal) is associated with changes in the W-O bond length, octahedral tilt, and/or displacement of the W atom out of the center of the octahedron [65,66]. The literature recognizes that the tetragonal α-WO_3 phase is less distorted than the monoclinic γ-WO_3 system because it presents lower tetrahedron tilting and W displacement from the octahedra center [66]. However, Wang *et al.* recently observed that the distortion imposed on the O_h-W sites by doping WO_3 with Rb atoms resulted in a longer W-O bond in the z-axis [65]. Therefore, the energy gap decrease observed throughout the δ → γ → β → α-WO_3 phase transition might be explained by the elongation of the W-O bond in the z-axis.

The energy gap of the T_d-W^{6+} sites narrows after the Na_2WO_4 melting (>698 °C) for Na_2WO_4/SiO_2 and widens in Mn-Na_2WO_4/SiO_2. Thus, although both catalysts have equal T_d-symmetry, the T_d-W sites on Mn-Na_2WO_4/SiO_2 exhibit a wider energy gap (2.2 vs. 1.6 eV at 800 °C), and therefore a lower distortion. After comparing the chemical, textural, and structural properties of these catalysts, it is evident that the exclusive presence of the O_h-Mn^{3+} sites in the molten Na_2WO_4 phase may be related to the lower distortion degree of the T_d-W sites observed for Mn-Na_2WO_4/SiO_2 catalyst. Recent studies have shown that Na^+ and WO_4^{2-} ions are unstable, mobile, and interact with other materials after Na_2WO_4 melting [24]. Thus, the interaction of the O_h-Mn^{3+} sites with the WO_4^{2-} ions (T_d-W^{6+} sites) will most likely be present on the catalyst surface wetted with the molten Na_2WO_4 phase. Finally, to confirm the presence of the O_h-Mn^{3+} sites and fully understand the molecular and electronic structure of the Mn-Na_2WO_4/SiO_2 catalyst at relevant OCM temperatures, we also performed *in situ* TPO-XANES spectroscopy at the Mn-K edge. Fig. 7 shows the *in situ*

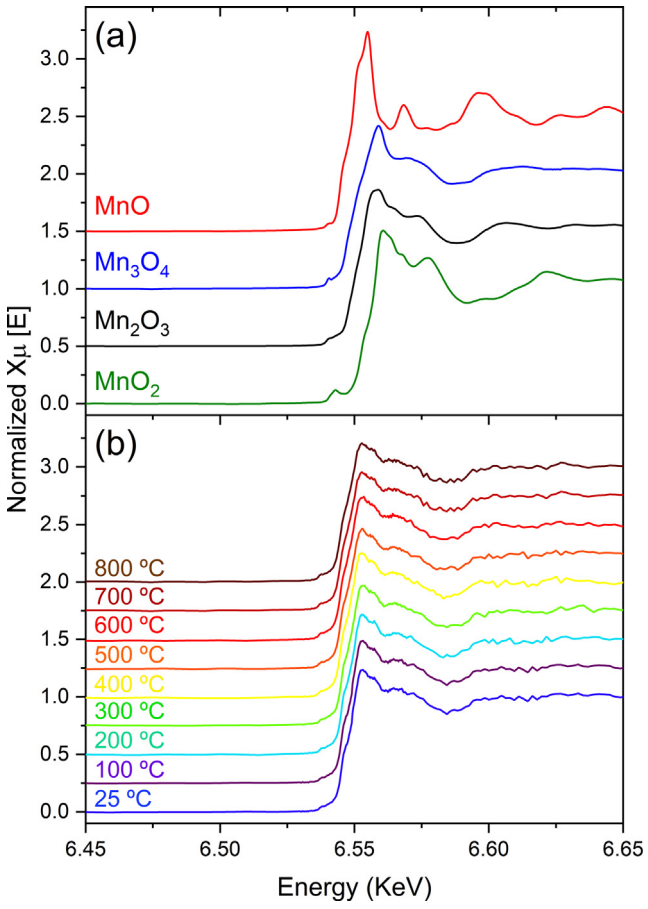

Fig. 7. *In situ* XANES spectra at the Mn-K edge of (a) reference materials at 25° C and (b) the Mn-Na_2WO_4/SiO_2 catalyst recorded between 25° C and 800° C (10° C min^{-1}) flowing O_2:He = 1:10 (10 $cm^3 \cdot min^{-1}$).

XANES spectra at the Mn-K edge of the bulk MnO, Mn_3O_4, Mn_2O_3, and MnO_2 reference materials recorded at 25 °C (Fig. 7a) and the Mn-Na_2WO_4/SiO_2 catalyst at increasing temperatures up to 800 °C (Fig. 7b).

We can easily observe that the Mn-K edge XANES spectra of the Mn-Na_2WO_4/SiO_2 catalyst resemble the spectra of bulk Mn_2O_3 reference material at 25 °C. Although the *in situ* TPO-Raman spectra of the Mn-Na_2WO_4/SiO_2 catalyst exhibits a band related to the mixed-valent hausmanite $Mn^{2+}Mn_2^{3+}O_4$ phase, the Mn^{3+} sites dominate the XANES spectrum. Upon heating, the Mn-K edge XANES spectra of the Mn-Na_2WO_4/SiO_2 catalyst keep almost unchanged, suggesting that Mn atoms are mostly present as O_h-Mn^{3+} sites at relevant OCM temperatures [24]. Therefore, O_h-Mn^{3+} and T_d-W^{6+} electronic states are the most likely cation configuration of the Mn and W sites on the conventional Mn-Na_2WO_4/SiO_2 catalyst at real OCM temperatures, just before methane admission into the reactor.

3.2. Steady-State OCM catalytic tests

Because the most drastic structural variations under oxidizing conditions of the T_d-W^{6+} sites were observed above 650 °C, the steady-state OCM catalytic tests were performed at 650, 700, 750, and 800 °C. Fig. 8 depicts the steady-state OCM performance in terms of methane conversion (X_{CH4}) and selectivity to C_2 hydrocarbons (S_{C2}) for WO_3/SiO_2, Na_2WO_4/SiO_2, and Mn-Na_2WO_4/SiO_2 catalysts and the blank test (an empty reactor with no catalyst under the same conditions), together with the phase transitions

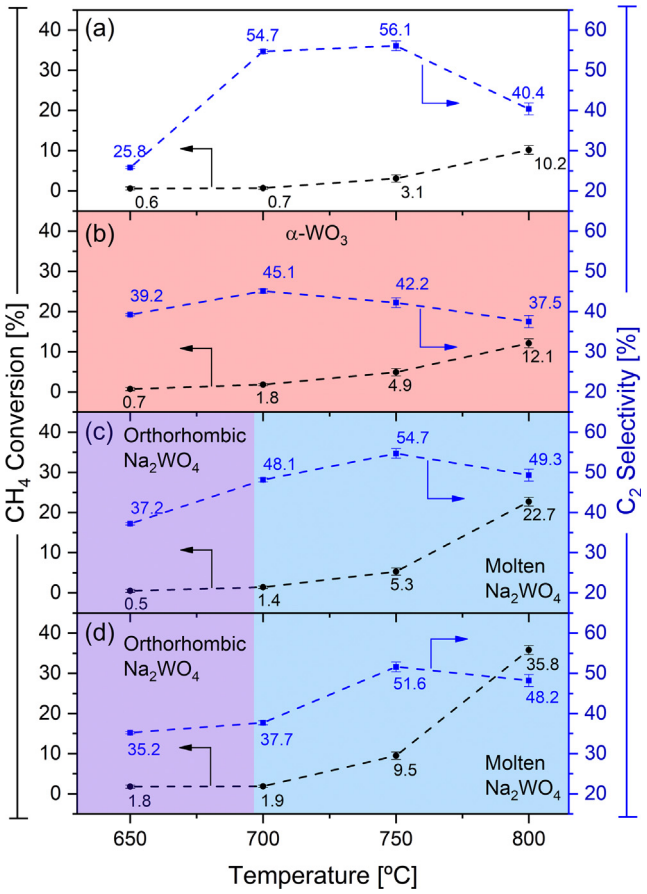

Fig. 8. Steady-state OCM performance tests using: (a) an empty reactor with no catalyst (blank test) and the (b) WO_3/SiO_2, (c) Na_2WO_4/SiO_2, and (d) Mn-Na_2WO_4/SiO_2 catalysts. Results acquired at 650, 700, 750, and 800° C flowing 73 $cm^3 \cdot min^{-1}$ of a mixture CH_4:O_2:He:N_2 (molar ratio 2:1:2:0.5) through ~ 0.1 g of catalyst diluted with 0.4 g of carborundum (180–250 μm).

of W sites evidenced in our TPO-XRD analysis. The blank test (homogeneous reaction) is selective, albeit not very active; the presence of catalytic materials affords higher conversions, being selectivity dependent on the specific catalyst composition. Thus, at 650 °C, all catalysts exhibit higher S_{C2} and similar X_{CH4} than the blank test (X_{CH4} = 0.6% and S_{C2} = 25.8%), excluding the Mn-Na_2WO_4/SiO_2 catalyst that exhibits a X_{CH4} = 1.8%, which is above the experimental error at this temperature (±0.4%). At 700 °C, the S_{C2} in the blank test increases to 54.7%, but the X_{CH4} remains almost negligible (0.7%), Fig. 8a; the WO_3/SiO_2 and Na_2WO_4/SiO_2 catalysts exhibit an increase in X_{CH4} (1.8 and 1.4%, respectively) and S_{C2} (45.1 and 48.1%, respectively), Fig. 8b-8c; and the Mn-Na_2WO_4/SiO_2 catalyst exhibits a slight increase in S_{C2} (37.7%), while the X_{CH4} remains unchanged (1.9%), Fig. 8d. The S_{C2} of the WO_3/SiO_2 and Na_2WO_4/SiO_2 catalysts was lower than in the homogeneous reaction due to the higher X_{CH4}, leading to sequential reactions towards undesired, more thermodynamically stable CO_x compounds [2]. The X_{CH4} of Mn-Na_2WO_4/SiO_2 and Na_2WO_4/SiO_2 catalysts is similar (within the experimental error at this temperature, ± 0.3%), but the S_{C2} of the Na_2WO_4/SiO_2 catalyst is significantly higher.

As the temperature reaches 750 °C, the blank test shows an increase in both X_{CH4} (3.1%) and S_{C2} (56.1%), Fig. 8a; the WO_3/SiO_2 catalyst shows an increase in X_{CH4} (4.9%) and a decrease in S_{C2} (42.2%), Fig. 8b; and the Na_2WO_4/SiO_2 and Mn-Na_2WO_4/SiO_2 catalysts exhibit an increase in both X_{CH4} (5.3 and 9.5%, respectively) and S_{C2} (54.7 and 51.6%, respectively), Fig. 8c-8d. The use of the WO_3/SiO_2 catalyst, compared to the blank test, results in a slightly higher X_{CH4} (from 3.1 to 4.9%) but a drastic decrease in S_{C2} (from 56.1% to 42.2%). Thus, the WO_3/SiO_2 sample is a poorly selective OCM catalyst, in agreement with the literature [12]. Actually, the octahedral coordination of the W^{6+} sites in the crystalline WO_3 phase has been related to deep oxidation reactions. This feature is even more evident at 800 °C (at higher X_{CH4}), Fig. 8b. Finally, all the catalysts and the blank test afforded higher X_{CH4} and lower S_{C2} at 800 °C. The Na_2WO_4/SiO_2 and Mn-Na_2WO_4/SiO_2 catalysts exhibited a similar S_{C2} (49.3 and 48.2%, respectively), within experimental error at this temperature (±1.2%), but the X_{CH4} of the Mn-Na_2WO_4/SiO_2 was significantly higher (35.8% *vs.* 22.7%), suggesting that its less distorted T_d-W^{6+} sites are more active towards methane activation than the highly distorted T_d-W^{6+} sites in the Na_2WO_4/SiO_2 catalyst. The reactivity of the W sites on the catalysts for methane activation can be also analyzed by comparing the TOF values at each temperature, Table 2.

The number of reacted moles of methane per mol of W per second was always higher on the Mn-Na_2WO_4/SiO_2 catalyst, reflecting the synergistic effect among the supported Mn, Na, W oxides, in agreement with the literature [6]. Multiple works have attempted to elucidate the catalytic contribution of each supported oxide by formulating mono-, bi-, and tri-component oxide catalysts [19,20] and evaluating their OCM performance using different approaches, for instance chemical looping experiments: the Mn-Na_2WO_4/SiO_2 catalyst performs OCM reaction by involving the lattice oxygen from reducible W^{6+} and Mn^{3+} cations in the absence of gas-phase oxygen; however, the catalyst structure drastically changes under methane flow, forming the crystalline $MnWO_4$ phase [21,67]. This phase, with O_h-Mn^{2+} and O_h-W^{6+} sites (*i.e.*, wolframite structure), has been associated with the catalyst reduction and deactivation [21]. Higher temperatures and very reducing conditions (high CH_4/O_2 molar ratios in steady-state operation) accelerate the $MnWO_4$ phase formation [67].

We have characterized the catalyst discriminating the oxidizing and temperature effects on the structure from the effect of the methane flow. However, the T_d-W^{6+} and O_h-Mn^{3+} sites observed just before methane admission into the reactor in the present study are expected to be also present in the steady-state OCM

Table 2
TOF values obtained for steady-state OCM reaction.

Catalyst	TOF [mol CH_4 ·mol W^{-1}·s^{-1}]			
	650 °C	700 °C	750 °C	800 °C
WO_3/SiO_2	0.009	0.022	0.060	0.148
Na_2WO_4/SiO_2	0.006	0.017	0.063	0.270
Mn-Na_2WO_4/SiO_2	0.021	0.023	0.113	0.424

operation, under CH_4 + O_2 flow, because: *i*) at the operating temperatures catalyst reduction/deactivation (associated with $MnWO_4$ formation) is slower than catalyst re-oxidation [68], *ii*) the CH_4/O_2 ratio used was low (*i.e.*, 2), *iii*) the Mn_2O_3 phase has been observed during *operando* OCM studies even at CH_4/O_2 ratios as high as 10 [67], and *iv*) the Mn-Na_2WO_4/SiO_2 catalyst has been reported to be stable for extended time on stream (450–1000 h) under CH_4 + O_2 flow [6]. Comparing the performance of Mn-Na_2WO_4/SiO_2 and Na_2WO_4/SiO_2, the higher methane conversion exhibited by the former appears due to the exclusive presence of the O_h-Mn^{3+} sites, which makes the T_d-W^{6+} sites less distorted. However, we may not currently discard that Mn and Na play a role in the activity of this catalyst.

4. Conclusions

The structure of the Mn-Na_2WO_4/SiO_2 catalyst is highly temperature-dependent and, thus, the association of any OCM activity with crystalline phases observed at room temperature is inadequate. *In situ* TPO-XRD analysis shows that the crystalline phases identified on the Mn-Na_2WO_4/SiO_2, Mn-free Na_2WO_4/SiO_2, and Mn- and Na-free WO_3/SiO_2 catalysts at room temperature do not exist at OCM temperatures (>700 °C). The $\gamma \rightarrow \beta \rightarrow \alpha$-$WO_3$, $\alpha \rightarrow \beta$-cristobalite, and cubic → orthorhombic → molten Na_2WO_4 phase transitions occur upon heating in oxidizing conditions. *In situ* TPO-Raman study shows that the O_h-W^{6+} sites in the WO_3/SiO_2 catalyst and the T_d-W^{6+} sites in the Na_2WO_4/SiO_2 and Mn-Na_2WO_4/SiO_2 catalysts undergo significant structural changes during these phase transitions, as evidenced by the shift of the symmetric stretching (ν_s) vibration band. The ν_s vibration band shift suggests variations in the bond order of the W sites by changes in their oxidation state or distortion degree or both. *In situ* TPO-XANES spectra indicate that the ν_s vibration band shift is due to changes in the distortion degree instead of oxidation state, which remains unchanged (W^{6+}) for all catalysts at heating. Additionally, *in situ* TPO-XANES spectra confirm the presence of O_h-Mn^{3+} sites in Mn-Na_2WO_4/SiO_2 catalyst even at relevant OCM temperatures, which reduces the T_d-W^{6+} sites distortion in the molten Na_2WO_4 phase compared with the Na_2WO_4/SiO_2 catalyst. Finally, steady-state OCM tests confirm that the O_h-W^{6+} sites are not active and the presence of the O_h-Mn^{3+} sites, and thus less distorted T_d-W^{6+} sites, makes the Mn-Na_2WO_4/SiO_2 catalyst more reactive towards methane activation.

Declaration of Competing Interest

The authors declare that they have no known competing financial interests or personal relationships that could have appeared to influence the work reported in this paper.

Acknowledgment

This study was financed in part by the Coordenação de Aperfeiçoamento de Pessoal de Nível Superior - Brasil (CAPES)- Finance Code 001. We acknowledge the Brazilian Synchrotron Light Laboratory (LNLS) at the National Center for Research in Energy and Materials (CNPEM) for making available beam-time under proposal XAFS2-20190152. C.A.O-B gratefully acknowledge the financial support of the CAPES (process No. 88887.368574/2019-00) and Fundação Carlos Chagas Filho de Amparo à Pesquisa do Estado do Rio de Janeiro (FAPERJ) (process No. E-26/200.785/2019) for scholarship grant. The Raman system was acquired with Spanish Ministry grant EQC2018-004839-P and co-funded by CSIC.

Appendix A. Supplementary data

Supplementary data to this article can be found online at https://doi.org/10.1016/j.jcat.2021.06.021.

References

[1] McFarland E. Unconventional Chemistry for Unconventional Natural Gas, Science (80). 338 (2012) 340–342 https://doi.org/10.1126/science.1226840.
[2] B.L. Farrell, V.O. Igenegbai, S. Linic, A Viewpoint on Direct Methane Conversion to Ethane and Ethylene Using Oxidative Coupling on Solid Catalysts, ACS Catal. 6 (2016) 4340–4346, https://doi.org/10.1021/acscatal.6b01087.
[3] G.E. Keller, M.M. Bhasin, Synthesis of ethylene via oxidative coupling of methane I. Determination of active catalysts, J. Catal. 73 (1982) 9–19, https://doi.org/10.1016/0021-9517(82)90075-6.
[4] Z. Stansch, L. Mleczko, M. Baerns, Comprehensive Kinetics of Oxidative Coupling of Methane over the La2O3/CaO Catalyst, Ind. Eng. Chem. Res. 36 (1997) 2568–2579, https://doi.org/10.1021/ie960562k.
[5] P. Schwach, X. Pan, X. Bao, Direct Conversion of Methane to Value-Added Chemicals over Heterogeneous Catalysts: Challenges and Prospects, Chem. Rev. 117 (2017) 8497–8520, https://doi.org/10.1021/acs.chemrev.6b00715.
[6] D. Kiani, S. Sourav, J. Baltrusaitis, I.E. Wachs, Oxidative Coupling of Methane (OCM) by SiO2-Supported Tungsten Oxide Catalysts Promoted with Mn and Na, ACS Catal. 9 (2019) 5912–5928, https://doi.org/10.1021/acscatal.9b01585.
[7] S. Arndt, T. Otremba, U. Simon, M. Yildiz, H. Schubert, R. Schomäcker, Mn–Na2WO4/SiO2 as catalyst for the oxidative coupling of methane. What is really known?, Appl Catal. A Gen. 425–426 (2012) 53–61, https://doi.org/10.1016/j.apcata.2012.02.046.
[8] J.C.W. Kuo, C.T. Kresge, R.E. Palermo, Evaluation of direct methane conversion to higher hydrocarbons and oxygenates, Catal. Today. 4 (1989) 463–470, https://doi.org/10.1016/0920-5861(89)85042-4.
[9] A. Cruellas, J.J. Bakker, M. van Sint Annaland, J.A. Medrano, F. Gallucci, Techno-economic analysis of oxidative coupling of methane: Current state of the art and future perspectives, Energy Convers. Manag. 198 (2019), https://doi.org/10.1016/j.enconman.2019.111789.
[10] X. Fang, S. Li, J. Lin, Y. Chu, Oxidative Coupling of Methane on W-Mn Catalysts, J. Mol. Catal. 6 (1992) 427–433.
[11] Z.C. Jiang, C.J. Yu, X.P. Fang, S.B. Li, H.L. Wang, Oxide/support interaction and surface reconstruction in the sodium tungstate(Na2WO4)/silica system, J. Phys. Chem. 97 (1993) 12870–12875, https://doi.org/10.1021/j100151a038.
[12] J. Wu, S. Li, The Role of Distorted WO4 in the Oxidative Coupling of Methane on Supported Tungsten Oxide Catalysts, J. Phys. Chem. 99 (1995) 4566–4568, https://doi.org/10.1021/j100013a030.
[13] J. Wu, S. Li, J. Niu, X. Fang, Mechanistic study of oxidative coupling of methane over Mn2O3-Na2WO4SiO2 catalyst, Appl. Catal. A Gen. 124 (1995) 9–18, https://doi.org/10.1016/0926-860X(94)00245-2.
[14] Z.C. Jiang, H. Gong, S.B. Li, Methane activation over Mn2O3-Na2WO4/SiO2 catalyst and oxygen spillover, Stud. Surf. Sci. Catal. 112 (1997) 481–490, https://doi.org/10.1016/S0167-2991(97)80872-5.
[15] D.J. Wang, M.P. Rosynek, J.H. Lunsford, Oxidative Coupling of Methane over Oxide-Supported Sodium-Manganese Catalysts, J. Catal. 155 (1995) 390–402, https://doi.org/10.1006/jcat.1995.1221.
[16] T.W. Elkins, H.E. Hagelin-Weaver, Characterization of Mn–Na2WO4/SiO2 and Mn–Na2WO4/MgO catalysts for the oxidative coupling of methane, Appl. Catal. A Gen. 497 (2015) 96–106, https://doi.org/10.1016/j.apcata.2015.02.040.
[17] A. Palermo, J.P. Holgado Vazquez, A.F. Lee, M.S. Tikhov, R.M. Lambert, Critical influence of the amorphous silica-to-cristobalite phase transition on the performance of Mn/Na2WO4/SiO2 catalysts for the oxidative coupling of methane, J. Catal. 177 (1998) 259–266, https://doi.org/10.1006/jcat.1998.2109.

[18] A. Palermo, J.P. Holgado Vazquez, R.M. Lambert, New efficient catalysts for the oxidative coupling of methane, Catal. Letters. 68 (2000) 191–196, https://doi.org/10.1023/A:1019072512423.
[19] S.F. Ji, T.C. Xiao, S.B. Li, L.J. Chou, B. Zhang, C. Xu, R. Hou, A.P.E. York, M.L.H. Green, Surface WO4 tetrahedron: the essence of the oxidative coupling of methane over M-W-Mn/SiO2 catalysts, J. Catal. 220 (2003) 47–56, https://doi.org/10.1016/S0021-9517(03)00248-3.
[20] S.F. Ji, T.C. Xiao, S.B. Li, C.Z. Xu, R.L. Hou, K.S. Coleman, M.L.H. Green, The relationship between the structure and the performance of Na-W-Mn/SiO2 catalysts for the oxidative coupling of methane, Appl. Catal. A Gen. 225 (2002) 271–284, https://doi.org/10.1016/S0926-860X(01)00864-X.
[21] M.J. Werny, Y. Wang, F. Girgsdies, R. Schlögl, A. Trunschke, Fluctuating Storage of the Active Phase in a Mn-Na 2 WO 4 /SiO 2 Catalyst for the Oxidative Coupling of Methane, Angew. Chemie. 132 (2020) 15031–15036, https://doi.org/10.1002/ange.202004778.
[22] J. Wang, L. Chou, B. Zhang, H. Song, J. Zhao, J. Yang, S. Li, Comparative study on oxidation of methane to ethane and ethylene over Na2WO4-Mn/SiO2catalysts prepared by different methods, J. Mol. Catal. A Chem. 245 (2006) 272–277, https://doi.org/10.1016/j.molcata.2005.09.038.
[23] S. Sadjadi, S. Jašo, H.R. Godini, S. Arndt, M. Wollgarten, R. Blume, O. Görke, R. Schomäcker, G. Wozny, U. Simon, Feasibility study of the Mn-Na2WO4/SiO2 catalytic system for the oxidative coupling of methane in a fluidized-bed reactor, Catal. Sci. Technol. 5 (2015) 942–952, https://doi.org/10.1039/c4cy00822g.
[24] A. Vamvakeros, D. Matras, S.D.M. Jacques, M. di Michiel, S.W.T. Price, P. Senecal, M.A. Aran, V. Middelkoop, G.B.G. Stenning, J.F.W. Mosselmans, I.Z. Ismagilov, A.M. Beale, Real-time multi-length scale chemical tomography of fixed bed reactors during the oxidative coupling of methane reaction, J. Catal. 386 (2020) 39–52, https://doi.org/10.1016/j.jcat.2020.03.027.
[25] A. Vamvakeros et al., Real time chemical imaging of a working catalytic membrane reactor during oxidative coupling of methane, Chem. Commun. 51 (2015) 12752–12755, https://doi.org/10.1039/c5cc03208c.
[26] D. Kiani, S. Sourav, I.E. Wachs, J. Baltrusaitis, Synthesis and molecular structure of model silica-supported tungsten oxide catalysts for oxidative coupling of methane (OCM), Catal. Sci. Technol. 10 (2020) 3334–3345, https://doi.org/10.1039/D0CY00289E.
[27] Y. Kou, B. Zhang, J. Niu, S. Li, H. Wang, T. Tanaka, S. Yoshida, Amorphous Features of Working Catalysts: XAFS and XPS Characterization of Mn/Na2WO4/SiO2 as used for the Oxidative Coupling of Methane, J. Catal. 173 (1998) 399–408, https://doi.org/10.1006/jcat.1997.1900.
[28] S.J.A. Figueroa, J.C. Mauricio, J. Murari, D.B. Beniz, J.R. Piton, H.H. Slepicka, M.F. de Sousa, A.M. Espíndola, A.P.S. Levinsky, Upgrades to the XAFS2 beamline control system and to the endstation at the LNLS, J. Phys. Conf. Ser. 712 (2016), https://doi.org/10.1088/1742-6596/712/1/012022.
[29] S.J.A. Figueroa, D. Gibson, T. Mairs, S. Pasternak, et al., Innovative insights in a plug flow microreactor for operando X-ray studies, J. Appl. Crystallogr. 46 (2013) 1523–1527, https://doi.org/10.1107/S0021889813018839.
[30] B. Ravel, M. Newville, ATHENA, ARTEMIS, HEPHAESTUS : data analysis for X-ray absorption spectroscopy using IFEFFIT, J. Synchrotron Radiat. 12 (2005) 537–541, https://doi.org/10.1107/S0909049505012719.
[31] T.P. Tiemersma, M.J. Tuinier, F. Gallucci, J.A.M. Kuipers, M.V.S. Annaland, A kinetics study for the oxidative coupling of methane on a Mn/Na2WO4/SiO2 catalyst, Appl. Catal. A Gen. 433–434 (2012) 96–108, https://doi.org/10.1016/j.apcata.2012.05.002.
[32] C. Mazzara, J. Jupille, A.-M. Flank, P. Lagarde, Stereochemical Order around Sodium in Amorphous Silica, J. Phys. Chem. B. 104 (2000) 3438–3445, https://doi.org/10.1021/jp9924474.
[33] H. Wang, R. Schmack, B. Paul, M. Albrecht, S. Sokolov, S. Rümmler, E.V. Kondratenko, R. Kraehnert, Porous silicon carbide as a support for Mn/Na/W/SiC catalyst in the oxidative coupling of methane, Appl. Catal. A Gen. 537 (2017) 33–39, https://doi.org/10.1016/j.apcata.2017.02.018.
[34] M. Yildiz, Y. Aksu, U. Simon, K. Kailasam, O. Goerke, F. Rosowski, R. Schomäcker, A. Thomas, S. Arndt, Enhanced catalytic performance of MnxOy–Na2WO4/SiO 2 for the oxidative coupling of methane using an ordered mesoporous silica support, Chem. Commun. 50 (2014) 14440–14442, https://doi.org/10.1039/C4CC06561A.
[35] S. Pak, J.H. Lunsford, Thermal effects during the oxidative coupling of methane over Mn/Na2WO4/SiO2 and Mn/Na2WO4/MgO catalysts, Appl. Catal. A Gen. 168 (1998) 131–137, https://doi.org/10.1016/S0926-860X(97)00340-2.
[36] U. Simon, O. Görke, A. Berthold, S. Arndt, R. Schomäcker, H. Schubert, Fluidized bed processing of sodium tungsten manganese catalysts for the oxidative coupling of methane, Chem. Eng. J. 168 (2011) 1352–1359, https://doi.org/10.1016/j.cej.2011.02.013.
[37] H.R. Godini, A. Gili, O. Görke, S. Arndt, U. Simon, A. Thomas, R. Schomäcker, G. Wozny, Sol–gel method for synthesis of Mn–Na2WO4/SiO2 catalyst for methane oxidative coupling, Catal. Today 236 (2014) 12–22, https://doi.org/10.1016/j.cattod.2014.01.005.
[38] J.G. Howell, Y.P. Li, A.T. Bell, Propene Metathesis over Supported Tungsten Oxide Catalysts: A Study of Active Site Formation, ACS Catal. 6 (2016) 7728–7738, https://doi.org/10.1021/acscatal.6b01842.
[39] K. Thummavichai, N. Wang, F. Xu, G. Rance, Y. Xia, Y. Zhu, In situ investigations of the phase change behaviour of tungsten oxide nanostructures, R. Soc. Open Sci. 5 (2018), https://doi.org/10.1098/rsos.171932.
[40] S. Pokhrel, J. Birkenstock, A. Dianat, J. Zimmermann, M. Schowalter, A. Rosenauer, L.C. Ciacchi, L. Mädler, In situ high temperature X-ray diffraction, transmission electron microscopy and theoretical modeling for the formation of WO3 crystallites, CrystEngComm. 17 (2015) 6985–6998, https://doi.org/10.1039/c5ce00526d.
[41] H. Wei, W. Leng, J. Song, M.R. Willner, L.C. Marr, W. Zhou, P.J. Vikesland, Improved Quantitative SERS Enabled by Surface Plasmon Enhanced Elastic Light Scattering, Anal. Chem. 90 (2018) 3227–3237, https://doi.org/10.1021/acs.analchem.7b04667.
[42] M. Boulova, G. Lucazeau, Crystallite Nanosize Effect on the Structural Transitions of WO3 Studied by Raman Spectroscopy, J. Solid State Chem. 167 (2002) 425–434, https://doi.org/10.1006/jssc.2002.9649.
[43] E.I. Ross-Medgaarden, I.E. Wachs, Structural Determination of Bulk and Surface Tungsten Oxides with UV−vis Diffuse Reflectance Spectroscopy and Raman Spectroscopy, J. Phys. Chem. C. 111 (2007) 15089–15099, https://doi.org/10.1021/jp074219c.
[44] J.B. Bates, Raman Spectra of α and β Cristobalite, J. Chem. Phys. 57 (1972) 4042–4047, https://doi.org/10.1063/1.1678878.
[45] F.D. Hardcastle, I.E. Wachs, Determination of the molecular structures of tungstates by Raman spectroscopy, J. Raman Spectrosc. 26 (1995) 397–405, https://doi.org/10.1002/jrs.1250260603.
[46] R090057 - RRUFF Database: Raman, X-ray, Infrared, and Chemistry, (n.d.). https://rruff.info/general=Braunite/display=default/R090057 (accessed April 3, 2021).
[47] F. Buciuman, F. Patcas, R. Craciun, D.R.T. Zahn, Vibrational spectroscopy of bulk and supported manganese oxides, PCCP 1 (1999) 185–190, https://doi.org/10.1039/a807821a.
[48] S.S. Data, S. References, Search Sample Data Us Search References About RRUFF Contact Natrolite R060561, Cell 1–2 (2009).
[49] J.A. Horsley, I.E. Wachs, J.M. Brown, G.H. Via, F.D. Hardcastle, Structure of surface tungsten oxide species in the WO3/Al2O3 supported oxide system from x-ray absorption near-edge spectroscopy and Raman spectroscopy, J. Phys. Chem. 91 (1987) 4014–4020, https://doi.org/10.1021/j100299a018.
[50] C.L. Lima, G.D. Saraiva, P.T.C. Freire, M. Maczka, W. Paraguassu, F.F. de Sousa, J. Mendes Filho, Temperature-induced phase transformations in Na2WO4 and Na2MoO4 crystals, J. Raman Spectrosc. 42 (2011) 799–802, https://doi.org/10.1002/jrs.2759.
[51] J. Wang, J. You, M. Wang, L. Lu, A.A. Sobol, S. Wan, In-situ high-temperature Raman spectroscopic studies of the vibrational characteristics and microstructure evolution of sodium tungstate dihydrate crystal during heating and melting, J. Raman Spectrosc. 49 (2018) 1693–1705, https://doi.org/10.1002/jrs.5429.
[52] Y. Iwasawa, K. Asakura, M. Tada, XAFS Techniques for Catalysts, Nanomaterials, and Surfaces, Springer International Publishing, Cham (2017), https://doi.org/10.1007/978-3-319-43866-5.
[53] O.Y. Khyzhun, XPS, XES and XAS studies of the electronic structure of tungsten oxides, J. Alloys Compd. 305 (2000) 1–6, https://doi.org/10.1016/S0925-8388(00)00697-6.
[54] F.J. Garcia-Garcia, J. Gil-Rostra, F. Yubero, J.P. Espinós, A.R. Gonzalez-Elipe, "In Operando" X-ray Absorption Spectroscopy Analysis of Structural Changes During Electrochemical Cycling of WO3 and WxSiyOz Amorphous Electrochromic Thin Film Cathodes, J. Phys. Chem. C. 119 (2015) 644–652, https://doi.org/10.1021/jp508377v.
[55] N.N. Greenwood, A. Earnshaw, Chemistry of the elements, 2 n.d.,., Butterworth-Heinemann, Oxford, 1998.
[56] E. Bousquet, H. Hamdi, P. Aguado-Puente, E.K.H. Salje, E. Artacho, P. Ghosez, First-principles characterization of single-electron polaron in WO 3, Phys. Rev. Res. 2 (2020) 1–5, https://doi.org/10.1103/physrevresearch.2.012052.
[57] E.K.H. Salje, Polaronic states and superconductivity in WO3-x, Condens. Matter. 5 (2020), https://doi.org/10.3390/condmat5020032.
[58] O.F. Schirmer, E. Salje, The W5+ polaron in crystalline low temperature WO3 ESR and optical absorption, Solid State Commun. 33 (1980) 333–336, https://doi.org/10.1016/0038-1098(80)91164-3.
[59] F. Dkhilalli, S. Megdiche, K. Guidara, M. Rasheed, R. Barillé, M. Megdiche, AC conductivity evolution in bulk and grain boundary response of sodium tungstate Na2WO4, Ionics (Kiel). 24 (2018) 169–180, https://doi.org/10.1007/s11581-017-2193-8.
[60] E.I. García-López, G. Marcì, I. Krivtsov, J. Casado Espina, L.F. Liotta, A. Serrano, Local Structure of Supported Keggin and Wells-Dawson Heteropolyacids and Its Influence on the Catalytic Activity, J. Phys. Chem. C. 123 (2019) 19513–19527, https://doi.org/10.1021/acs.jpcc.9b03659.
[61] S. Yamazoe, Y. Hitomi, T. Shishido, T. Tanaka, XAFS Study of Tungsten L1 - and L3-Edges: Structural Analysis of WO3 Species Loaded on TiO2 as a Catalyst for Photo-oxidation of NH3, J. Phys. Chem. C 112 (2008) 6869–6879, https://doi.org/10.1021/jp711250f.
[62] H. Asakura, T. Shishido, S. Yamazoe, K. Teramura, T. Tanaka, Structural Analysis of Group V, VI, and VII Metal Compounds by XAFS, J. Phys. Chem. C. 115 (2011) 23653–23663, https://doi.org/10.1021/jp2034104.

[63] A. Balerna, E. Bernieri, E. Burattini, A. Kuzmin, A. Lusis, J. Purans, P. Cikmach, EXAFS studies of MeO3−x (Me = W, Mo, Re, Ir) crystalline and amorphous oxides, Nucl. Instruments Methods Phys. Res. Sect. A Accel. Spectrometers, Detect. Assoc. Equip. 308 (1991) 234–239, https://doi.org/10.1016/0168-9002(91)90636-5.

[64] M.V. Limaye et al., Correlation between electrochromism and electronic structures of tungsten oxide films, RSC Adv. 4 (2014) 5036–5045, https://doi.org/10.1039/c3ra45421e.

[65] Y.C. Wang, C.H. Hsu, Y.Y. Hsu, C.C. Chang, C.L. Dong, T.S. Chan, K. Kumar, H.L. Liu, C.L. Chen, M.K. Wu, Structural distortion and electronic states of Rb doped WO 3 by X-ray absorption spectroscopy, RSC Adv. 6 (2016) 107871–107877, https://doi.org/10.1039/C6RA21777J.

[66] T. Vogt, P.M. Woodward, B.A. Hunter, The High-Temperature Phases of WO3, J. Solid State Chem. 144 (1999) 209–215, https://doi.org/10.1006/jssc.1999.8173.

[67] P. Wang, G. Zhao, Y. Wang, Y. Lu, MnTiO 3 -driven low-temperature oxidative coupling of methane over TiO 2 -doped Mn 2 O 3 -Na 2 WO 4 /SiO 2 catalyst, Sci. Adv. 3 (2017), https://doi.org/10.1126/sciadv.1603180.

[68] Y. Gordienko, T. Usmanov, V. Bychkov, V. Lomonosov, Z. Fattakhova, Y. Tulenin, D. Shashkin, M. Sinev, Oxygen availability and catalytic performance of NaWMn/SiO2 mixed oxide and its components in oxidative coupling of methane, Catal. Today. 278 (2016) 127–134, https://doi.org/10.1016/j.cattod.2016.04.021.